Nanoscale

PAPER

Cite this: *Nanoscale*, 2015, **7**, 7833

Motion-based threat detection using microrods: experiments and numerical simulations†

Barath Ezhilan,[a] Wei Gao,[b] Allen Pei,[b] Isaac Rozen,[b] Renfeng Dong,[b] Beatriz Jurado-Sanchez,[b] Joseph Wang*[b] and David Saintillan*[a]

Received 21st October 2014,
Accepted 23rd March 2015

DOI: 10.1039/c4nr06208f

www.rsc.org/nanoscale

Motion-based chemical sensing using microscale particles has attracted considerable recent attention. In this paper, we report on new experiments and Brownian dynamics simulations that cast light on the dynamics of both passive and active microrods (gold wires and gold–platinum micromotors) in a silver ion gradient. We demonstrate that such microrods can be used for threat detection in the form of a silver ion source, allowing for the determination of both the location of the source and concentration of silver. This threat detection strategy relies on the diffusiophoretic motion of both passive and active microrods in the ionic gradient and on the speed acceleration of the Au–Pt micromotors in the presence of silver ions. A Langevin model describing the microrod dynamics and accounting for all of these effects is presented, and key model parameters are extracted from the experimental data, thereby providing a reliable estimate for the full spatiotemporal distribution of the silver ions in the vicinity of the source.

1 Introduction

Controlled migration and self-propulsion of microscale particles is a challenging task with a broad range of technological and biomedical applications. A classical way to manipulate colloidal suspensions relies on phoretic transport, by which externally imposed gradients of various fields (such as temperature, electric field, solute concentration *etc.*) can lead to the migration of colloidal particles. Recent advances in microfluidic technologies have spurred a renewed interest in the theoretical understanding and practical application of such transport mechanisms.[1,2]

In recent years, phoretic effects have also been used for the autonomous self-propulsion of microparticles. Catalytically active microparticles such as bimetallic microrods can indeed self-generate and sustain surface asymmetries leading to their propulsion through a variety of self-phoretic mechanisms.[3] These artificial micromotors offer a broad range of potential applications ranging from drug delivery, microscale assembly and transport, robotics, to motion-based chemical/biochemical sensing.[4–18] Potential environmental applications of micromotors have grown rapidly in recent years, indicating a myriad of innovative remediation and monitoring applications based on new motion-based phenomena.[19–24] Specifically, micromotors that exhibit a concentration dependence of their self-propulsion velocities could mimic chemotactic search strategies employed by microorganisms in biological settings and hence be used to trace plumes of hazardous chemicals to their source. Recently, Gao *et al.*[25] reported that Ir/silica Janus micromotors, powered by extremely low levels of hydrazine fuel, display a well-defined concentration/speed dependence, thus holding considerable promise for tracing concentration gradients of this pollutant. Experiments have shown that Au–Pt micromotors exhibit directed movement toward high hydrogen peroxide concentrations through 'active diffusion.'[26] In addition, an unusual speed acceleration of Au–Pt micromotors in the presence of silver ions has also been reported.[27] This specific unexpected effect of silver upon the speed of catalytic micromotors has been exploited for designing a new motion-based trace silver sensing protocol. The specific acceleration has been attributed to the underpotential deposition of silver onto a platinum segment, which increases the electrocatalytic activity. The highly selective motion-based response is characterized by a defined concentration dependence, with the speed of the micromotors providing quantitative information down to the nanomolar level. This silver-based acceleration has also formed the basis for a motion-based detection of DNA hybridization in connection to silver nanoparticle tags.[28]

While previous studies have separately focused on phoretic migration in an external gradient and on self-phoretic propulsion in the absence of external gradients, the combined use of both transport strategies has been widely unexplored and could lead to novel avenues for the control of colloidal

[a]*Department of Mechanical and Aerospace Engineering, University of California San Diego, 9500 Gilman Drive, La Jolla, CA 92093, USA. E-mail: dstn@ucsd.edu*
[b]*Department of Nanoengineering, University of California San Diego, 9500 Gilman Drive, La Jolla, CA 92093, USA. E-mail: josephwang@ucsd.edu*
†Electronic supplementary information (ESI) available. See DOI: 10.1039/c4nr06208f

motions or the sensing of external fields. Because of the ubiquity of Brownian motion at the length scales relevant to these suspensions, the non-trivial interplay of phoretic migration, self-phoretic propulsion and Brownian fluctuations is of significant theoretical and practical interest. In the context of biological transport, this is analogous to the coupling between swimming, chemotactic migration and Brownian motion, which is known to lead to a rich variety of non-trivial phenomena.

In this paper, we perform experiments using both passive tracers (Au microwires) and active swimmers (Au–Pt microwires) near a silver ion source using methods described in section 2. Passive tracers in an electrolyte gradient move towards lower concentration of electrolyte as explained by classical theories of diffusiophoresis.[29,30] This effect causes a marked depletion of gold microwires near the silver ion source, thus enabling spatial detection of the source. Active swimmers (Au–Pt microwires) also exhibit a diffusiophoretic response to the externally imposed silver ion gradient (similar to passive tracers) while additionally accelerating in regions of higher silver ion concentration.[27] This silver-based acceleration characteristic of Au–Pt micromotors is utilized to develop a strategy for accurate spatiotemporal sensing of the silver ion concentration in the domain by fitting experimental data to a numerical model. In section 3, we introduce a Langevin model and Brownian Dynamics (BD) simulation methodology to analyze the non-trivial coupling of diffusiophoresis, silver-ion induced speed acceleration and Brownian motion. Key model parameters are extracted from the experimental velocity data of both passive tracers and active swimmers, from which the spatiotemporal evolution of the silver ion concentration in the domain is deduced. Results from the experiments and BD simulations are reported in section 4 where the spatiotemporal dynamics, density and velocity profiles of both passive tracers and active swimmers are analyzed in detail. We conclude in section 5.

2 Experimental methods

2.1 Micromotor preparation

The Au–Pt microwires were prepared by sequential electrodeposition of gold and platinum into 200 nm diameter cylindrical pores of an alumina membrane template (catalog no. 6809-6022; Whatman, Maidstone, U.K.). A thin gold film was first sputtered on the branched side of the membrane to serve as a working electrode. The membrane was assembled in a Teflon plating cell with aluminum foil serving as an electrical contact for the subsequent electrodeposition. A sacrificial copper layer was first electrodeposited into the branched area of the membrane using a 1 M cupric sulfate pentahydrate solution ($CuSO_4 \cdot 5H_2O$; Sigma-Aldrich, St. Louis, MO), at total charge of 10 °C and a potential of −1.0 V (*vs.* Ag/AgCl reference electrode) along with platinum wire as a counter electrode. Subsequently, a Au segment was plated from a gold plating solution (Orotemp 24 RTU RACK; Technic Inc., Anaheim, CA) and electrodeposited at a total charge of 1.5 °C and a potential of −0.9 V. Platinum was then deposited galvanostatically using a current of −2 mA for 50 min from a platinum plating solution (Platinum RTP; Technic Inc.). The resulting Au–Pt microwires had a length of around 2 μm. The sputtered gold layer and the copper sacrificial layer were simultaneously removed by mechanical polishing with 3–4 μm alumina slurry. The bisegment Au/Pt microwires were then released by immersing the membrane in 3 M NaOH for 30 min. The synthesized micromotors were separated from solution by centrifugation at 10 000 rpm for 5 min and washed repeatedly with ultrapure water (18.2 MΩ cm) until a neutral pH was achieved. Between the washing steps, the micromotor solution was mixed with ultrapure water and briefly sonicated (25 s) to ensure the complete dispersion of micromotors. All micromotors were stored in ultrapure water at room temperature and their speed was tested before each experiment.

2.2 Silver ion source preparation

Planar sources of elemental silver were fabricated through a photolithographic process. After patterning 50 μm cylindrical wells in a photoresist film on a glass coverslip, 10 nm of Ti and 100 nm of Ag were deposited onto the glass by electron beam evaporation (Temescal BJD 1800 E-beam Evaporator). The remaining metal film and underlying photoresist were stripped off in acetone, resulting in well-defined Ag films to serve as sources of Ag^+ ions. For the duration of the experiments, these Ag films can be considered as infinite sources, since they continuously release Ag^+ ions in the presence of hydrogen peroxide.

2.3 Setup

A schematic of the experimental setup is shown in Fig. 1. A known volume of a solution containing the Au–Pt microwires

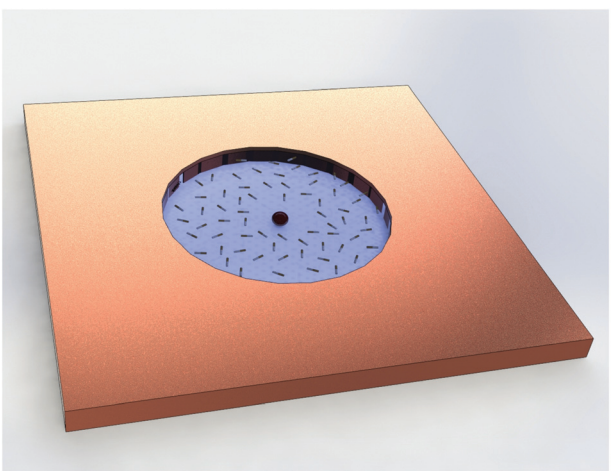

Fig. 1 (color online) Schematic of the experimental setup. Silver source (black dot in the center) releases Ag^+ into a fuel enhanced (0.1% hydrogen peroxide) solution containing Au–Pt active microwires or Au passive microwires. The movement of the micromotors was followed using an inverted microscope.

was dropped onto the planar silver source. The wires were allowed to settle in the plane of focus before the same volume of hydrogen peroxide fuel (0.1%), essential for microwire propulsion and silver dissolution, was added using a pipette. Control experiments performed with an inert source made of glass (instead of the active silver ion source) showed no convective perturbations or phoretic drift due to the transient inhomogeneities in the mixing process. This suggests that the peroxide and microrod solutions mix rapidly on timescales significantly higher than the phoretic timescales relevant to our problem. Based on their self-electrophoretic mechanism, the micromotors self-propel at a speed of 10 μm s^{-1} in a 0.1% hydrogen peroxide solution. This micromotor speed increases dramatically in the presence of Ag^{+} ions. Micromotor speeds were determined with movies taken at 45 frames per second using NIS-Elements AR software (Nikon, USA). Individual micromotor trajectories were tracked and Origin software was used to analyze the data.

2.4 Data extraction

2.4.1 Velocity tracking. The time of fuel addition to the microwire sample was taken to be the start of the experiment ($t = 0$). microwire velocities were tracked at 0 s, 2.5 s, 5 s, 10 s, 15 s, and 20 s after adding hydrogen peroxide and were averaged over 10 frames for each time interval. The distance of each micromotor from the center of the Ag source was recorded at the beginning of the 10-frame interval. Over 150 micromotors were tracked per time interval per video for 3 movies.

2.4.2 Density measurements. Density measurements were made at 0 s, 2.5 s, 5 s, 10 s and 20 s after fuel addition. A known volume of solution containing the Au–Pt microwires (for experiments with active tracers) or Au microwires (for experiments with passive tracers) was dropped onto the silver source. The swimmers/tracers were allowed to fully settle to the plane of focus before addition of the hydrogen peroxide fuel (0.1%). Rings with radii ranging from 25 μm to 125 μm and with spacing $\Delta r = 5$ μm between them were defined on the captured images at the specified times. The number of microwires within each consecutive pair of rings was counted, divided by the area, normalized by the initial number of microwires (at $t = 0$) and ensemble-averaged over 3 movies to obtain the wire density at discrete radial positions $r_j = [25 + (j - 0.5)\Delta r]$ μm for $j = 1...20$ using the following expression:

$$c(r_j,t) = \left\langle \frac{\sum_{i=1}^{N}\left[\int_{r_j-\frac{\Delta r}{2}}^{r_j+\frac{\Delta r}{2}}\delta(r-r_i)\,\mathrm{d}r\right]}{N(t=0)\pi\left[\left(r_j+\frac{\Delta r}{2}\right)^2-\left(r_j-\frac{\Delta r}{2}\right)^2\right]}\right\rangle, \quad (1)$$

where r_i is the radial position of each particle, $N(t = 0)$ is the total number of particles at the time of fuel addition ($t = 0$) and the symbol $\langle\cdot\rangle$ denotes an ensemble average over 3 distinct realizations of the experiment.

3 Langevin model and Brownian dynamics simulation

3.1 Particle fluxes

We describe the two-dimensional dynamics of $M = 1000$ particles (either passive tracers or active swimmers) using a Langevin model. A particle with index 'i' ($1 \le i \le M$) has center-of-mass position $\boldsymbol{x}_i$ and orientation $\boldsymbol{p}_i$ parametrized in the plane of motion as $\boldsymbol{p}_i = [\cos\theta_i, \sin\theta_i]$. During a short time interval δt, the center-of-mass displacement is calculated using the following Langevin equation as the sum of self-propulsive, diffusiophoretic and Brownian contributions:

$$\delta\boldsymbol{x}_i = \left[V_{\mathrm{sp}}(s[\boldsymbol{x}_i,t])\,\boldsymbol{p}_i + V_{\mathrm{dp}}(s[\boldsymbol{x}_i,t])\,\hat{\boldsymbol{e}}_{\mathrm{r}}\right]\delta t + \sqrt{2\boldsymbol{D}_{\mathrm{t}}\delta t}\cdot\boldsymbol{n}_1, \quad (2)$$

where $\hat{\boldsymbol{e}}_{\mathrm{r}} = \boldsymbol{x}_i/|\boldsymbol{x}_i|$ is a unit vector pointing radially outward from the position of the source at the center of particle i. Brownian fluctuations also lead to changes in the particle orientations, which are also captured by a Langevin equation:

$$\delta\boldsymbol{p}_i = \sqrt{2d_{\mathrm{r}}\delta t}(\boldsymbol{I}-\boldsymbol{pp})\cdot\boldsymbol{n}_2. \quad (3)$$

In eqn (2) and (3), $\boldsymbol{n}_1$ and $\boldsymbol{n}_2$ denote two-dimensional random vectors whose components follow a random Gaussian distribution with zero mean and unit variance. The translational and rotational diffusivities $\boldsymbol{D}_{\mathrm{t}}$ and d_{r} can be estimated for rod-like particles[31] as:

$$\boldsymbol{D}_{\mathrm{t}} = D_{\mathrm{t}}(\boldsymbol{I}+\boldsymbol{pp}) \text{ where } D_{\mathrm{t}} = \frac{k_{\mathrm{B}}T\,\log\left(\frac{1}{\varepsilon}\right)}{4\pi\mu\ell} \quad (4)$$

$$d_{\mathrm{r}} = \frac{3k_{\mathrm{B}}T\,\log\left(\frac{1}{\varepsilon}\right)}{\pi\mu\ell^3} \quad (5)$$

where ℓ and ε denote the length and inverse aspect ratio of a particle, respectively, and μ is the viscosity of the suspending fluid. The micromotors have a length of 2 μm and aspect ratio of ≈10. Based on these values, we estimate the Brownian translational diffusivity coefficient to be $D_{\mathrm{t}} \approx 4\times10^{-13}$ m^2 s^{-1}, and the rotational diffusivity to be $d_{\mathrm{r}} \approx 1$ s^{-1}.

V_{sp} and V_{dp} are the self-propulsive and diffusiophoretic velocities of the catalytic micromotors, which both depend on the evolving silver ion concentration $s[\boldsymbol{x}_i,t]$ in the domain. The functional dependence of the self-propulsion velocity on the silver concentration is obtained by fitting a logarithmic curve to the micromotor speed *vs.* silver ion concentration data of Kagan *et al.*:[27]

$$V_{\mathrm{sp}}(s) = \begin{cases} V_0 = 10\,\mu\mathrm{m\ s^{-1}}, & \text{if } s < 3.4\times10^{-7} \\ 7.1169\,\log(s) + 116.05, & \text{otherwise} \end{cases} \quad (6)$$

where s should be expressed in Molar units. To simulate the dynamics of passive tracers (Au microwires), we simply set $V_{\mathrm{sp}} = 0$.

The diffusiophoretic slip velocity of a spherical object in an ionic gradient was previously derived[29,30] and is expressed as:

$$V_{\mathrm{dp}}(s) = -D_{\mathrm{dp}}\frac{\partial\,\log\,s}{\partial r}, \quad (7)$$

where the coefficient D_{dp} is the sum of 'chemiphoretic' and 'electrophoretic' contributions:

$$D_{dp} = \frac{k_B T}{\mu}\kappa^{-2}\left[\nu_c(\zeta) + \tilde{\beta}\zeta\nu_e\right]. \quad (8)$$

here, ν_e and ν_c are positive coefficients, κ is the adsorption length, $\tilde{\beta}$ is the difference between anion and cation mobilities normalized by their sum, and ζ is the surface zeta potential. This peculiar 'log-sensing' property was also verified by recent experiments on diffusiophoresis in controlled electrolyte gradients.[1,2] We assume in our simulations that D_{dp} is a constant independent of the silver concentration, and the weak dependence of D_{dp} on salt concentration was indeed shown by Palacci *et al.*[1] to play only a minimal role. The simpler scaling for $D_{dp} \sim k_B T/\mu l_B$ has also been suggested,[32] where l_B is the Bjerrum length (l_B = 0.7 nm in water). This estimate gives $D_{dp} \approx 10^{-9}$ m^2 s^{-1} and $V_{dp} \sim D_{dp}/R_0 \approx 40$ μm s^{-1}. As we shall see in section 3, a more reliable estimate for D_{dp}/R_0 can in fact be extracted from the experimental data.

3.2 Silver ion evolution

In order to integrate eqn (2) and (3) in time, we require knowledge of the silver concentration field $s(\boldsymbol{x},t)$, which varies both in space and time. Specifically, silver ions diffuse radially into the domain from the boundary of the infinite silver source located at $r = R_0$ = 25 μm. We consider a finite-size computational domain of exterior radius R_{domain} = 150 μm. Silver ions are injected into the domain by the following surface reaction:

$$Ag(s) + H_2O_2 \rightarrow 2Ag^+(aq.) + 2OH^-. \quad (9)$$

At the surface of the source, we expect the rate j_0 of silver ion produced by the surface reaction to balance the diffusive flux away from the source:

$$-D_s \left.\frac{\partial s}{\partial r}\right|_{r=R_0} = j_0, \quad (10)$$

where D_s is the silver ion diffusivity and is set to 1.6×10^{-9} m^2 s^{-1} (diffusivity of silver ions in water). The silver ion flux j_0 at the source surface is expected to depend on the rate constant of the reaction and on the concentration of hydrogen peroxide near the surface: its value is not known *a priori* but will be extracted from the experimental data as explained in more detail in section 3.

A second boundary condition for the silver concentration is provided far away from the source:

$$s \rightarrow 0 \text{ at } r \rightarrow \infty, \quad (11)$$

and in practice we enforce this condition at $r = R_{domain}$.

Assuming an axisymmetric distribution, the evolution of the concentration of silver ions $s(r,t)$ inside this domain is governed by the diffusion equation, in spherical coordinates:

$$\frac{\partial s}{\partial t} = \frac{D_s}{r^2}\frac{\partial}{\partial r}\left(r^2\frac{\partial s}{\partial r}\right), \quad (12)$$

subject to boundary conditions (10) and (11). Solving this equation analytically using Laplace transforms, we derive the solution for the normalized silver ion concentration as a function of radial position and time:

$$\frac{s(r,t)}{j_0 R_0} = \frac{R_0}{D_s r}\left[\operatorname{erfc}\left(\frac{r-R_0}{2\sqrt{D_s t}}\right) - \exp\left(\frac{D_s t}{R_0^2} + \frac{r}{R_0} - 1\right)\operatorname{erfc}\left(\frac{\sqrt{D_s t}}{R_0} + \frac{r-R_0}{2\sqrt{D_s t}}\right)\right]. \quad (13)$$

At long times $t \gg R_0^2/D_s$, the normalized silver ion concentration profile reaches a steady state given by:

$$\frac{s^s(r)}{j_0 R_0} = \lim_{t\rightarrow\infty}\frac{s(r,t)}{j_0 R_0} = \frac{R_0}{r}. \quad (14)$$

Fig. 2(a) shows the normalized silver ion concentration profiles according to eqn (13) at different times t. It can be seen that, as time increases, the normalized silver ion concentration on the source surface ($r = R_0$) increases, asymptotically reaching a value of 1 at infinite time: $s(R_0,\infty) = j_0 R_0$. The concentration of silver ion in the domain also gradually increases everywhere as a result of diffusion.

Using the solution of eqn (13) for the silver ion concentration, we calculate the diffusiophoretic velocity $V_{dp}(s)$ as follows:

$$V_{dp} = \frac{D_{dp}}{R_0}\left[\frac{R_0}{r} - 1 + \left(1 - \frac{\exp\left(\frac{D_s t}{R_0^2} + \frac{r}{R_0} - 1\right)\operatorname{erfc}\left(\frac{\sqrt{D_s t}}{R_0} + \frac{r-R_0}{2\sqrt{D_s t}}\right)}{\operatorname{erfc}\left(\frac{r-R_0}{2\sqrt{D_s t}}\right)}\right)^{-1}\right]. \quad (15)$$

At long times $t \gg R_0^2/D_s$, the diffusiophoretic velocity also reaches a steady state given by:

$$V_{dp}^s(r) = \lim_{t\rightarrow\infty} V_{dp}(r,t) = \frac{D_{dp}}{r}. \quad (16)$$

The spatial dependence of the diffusiophoretic velocity at different times is illustrated in Fig. 2(b), showing the logarithm of the silver ion concentration profile. At short times,

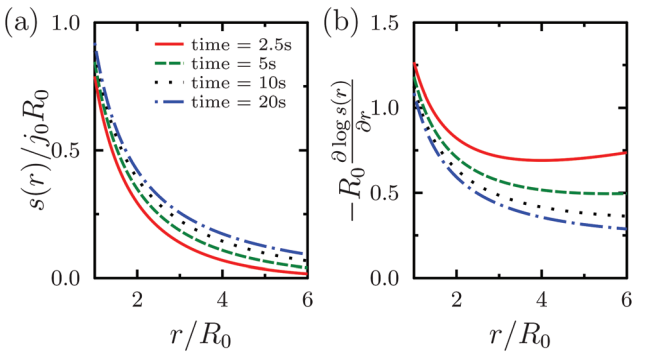

Fig. 2 (color online) (a) Normalized silver ion concentration profile and (b) its logarithm as a function of radial position and time.

when the silver ions have not yet diffused significantly into the domain ($s \to 0$), the model of eqn (15) predicts a nonphysical increase in the logarithmic silver ion profile. To remedy this, we set V_{dp} to zero when the silver concentration s fall below the critical value of $s_{min} = 0.2 j_0 R_0$, which suppresses the nonphysical increase of $\partial \log s/\partial r$ with r in limit of $s \to 0$. A similar method was previously used by Hong *et al.*[33]

3.3. Model parameter extraction

The model described above has two unknown parameters: the diffusiophoretic coefficient D_{dp}, and the surface silver ion flux j_0 on the surface of the source. As we explain here, both of these parameters can be extracted from the experimental data, using two sets of experiments involving passive particles and active micromotors. First, it can be noticed that while the self-propulsion velocity V_{sp} in eqn (6) depends on the surface ion flux j_0, the diffusiophoretic velocity V_{dp} in eqn (15) does not and only involves D_{dp}. This implies that D_{dp} can first be extracted from data for passive particles (Au microwires). Such data for the velocity *vs.* distance from the source is shown in Fig. 3(a), and can be fit to the model of eqn (15) to obtain the estimate $D_{dp}/R_0 = 10\ \mu m\ s^{-1}$. Once D_{dp} is known, the active micromotor (Au–Pt microwire) data, shown in Fig. 3(b), can then be used to obtain the best fit value of $j_0 R_0 = 2.52 \times 10^{-6}$ M for the silver ion flux. This estimate for $j_0 R_0$, coupled with the analytical solution of eqn (13), enables prediction of the full spatiotemporal silver ion concentration profile throughout the domain with good resolution.

3.4 Simulation method

At $t = 0$, the particle positions and orientations are initialized with a uniform isotropic distribution. The governing equations are non-dimensionalized using the following scales for lengths, time, and silver concentration:

$$L_c = R_0 = 25\ \mu m, \tag{17}$$

$$t_c = \frac{R_0^2}{D_s} \approx 0.4\ s, \tag{18}$$

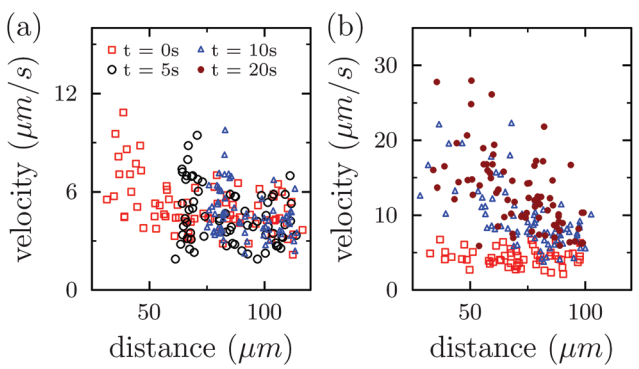

Fig. 3 (color online) Experimental data showing velocity as a function of radial position and time for (a) active swimmers (Au–Pt micromotors) and (b) passive tracers (Au microwires).

$$s_c = j_0 R_0. \tag{19}$$

The self-propulsion and diffusiophoretic contributions to the translational flux can be calculated analytically using eqn (6) and (15). Time integration of the Langevin equations for the particle motions are performed using a second-order Adams–Bashforth time-marching scheme. The swimmer/tracer density profiles were calculated in the same fashion as the experimental profile measurement described in section 2, but ensemble-averaged over 12 simulation runs.

3.5 Model assumptions and limitations

The model described above is the simplest model that accounts for all relevant effects including self-propulsion, diffusiophoresis, and diffusion of silver ions. However, it is also based on a number of simplifications and approximations that may have a quantitative impact on the results. First, we note that the classical expression for the diffusiophoretic velocity used here was originally derived for spherical particles.[29,30] While we do not expect the dependence on s to change significantly for rod-like particles such as the micromotors considered here, diffusiophoresis may also lead to a rotational flux contribution, though this flux is negligible unless strong gradients exist on the scale of the particles, which is not the case here. Second, we have neglected the effect of the microrods on the distribution of silver ions. This effect can be twofold: on the one hand, the reaction of the silver ions with the microrods is expected to deplete the silver concentration in their vicinity; on the other hand, motion of the particles may also lead to convection and stirring of the silver ions beyond the simple effect of molecular diffusion. Finally we note that we have ignored both steric and hydrodynamic interactions between micromotors on the basis that the suspensions used in the experiments were dilute; these interactions may play a minor role in the fronts that form near the silver source, where the density is higher, yet we do not expect them to significantly modify the results.

4 Results and discussion

As the fuel is added at $t = 0$, the silver ions are produced on the surface of the source at $r = R_0$ and rapidly diffuse into the domain (as shown in Fig. 2). This drives the formation of silver ion gradients in the domain, to which both passive tracers and active micromotors respond in unique ways as explained below.

4.1 Passive tracer dynamics

The spatiotemporal dynamics of passive tracers are illustrated in Fig. 4(a) and (b) (and accompanying video). Over time, the tracers progressively move away from the source due to diffusiophoresis. This results in the complete depletion of tracers near the source. As shown in the passive tracer density profiles in Fig. 5, a sharply defined depletion front progresses radially outward over time. The interface between the depletion region

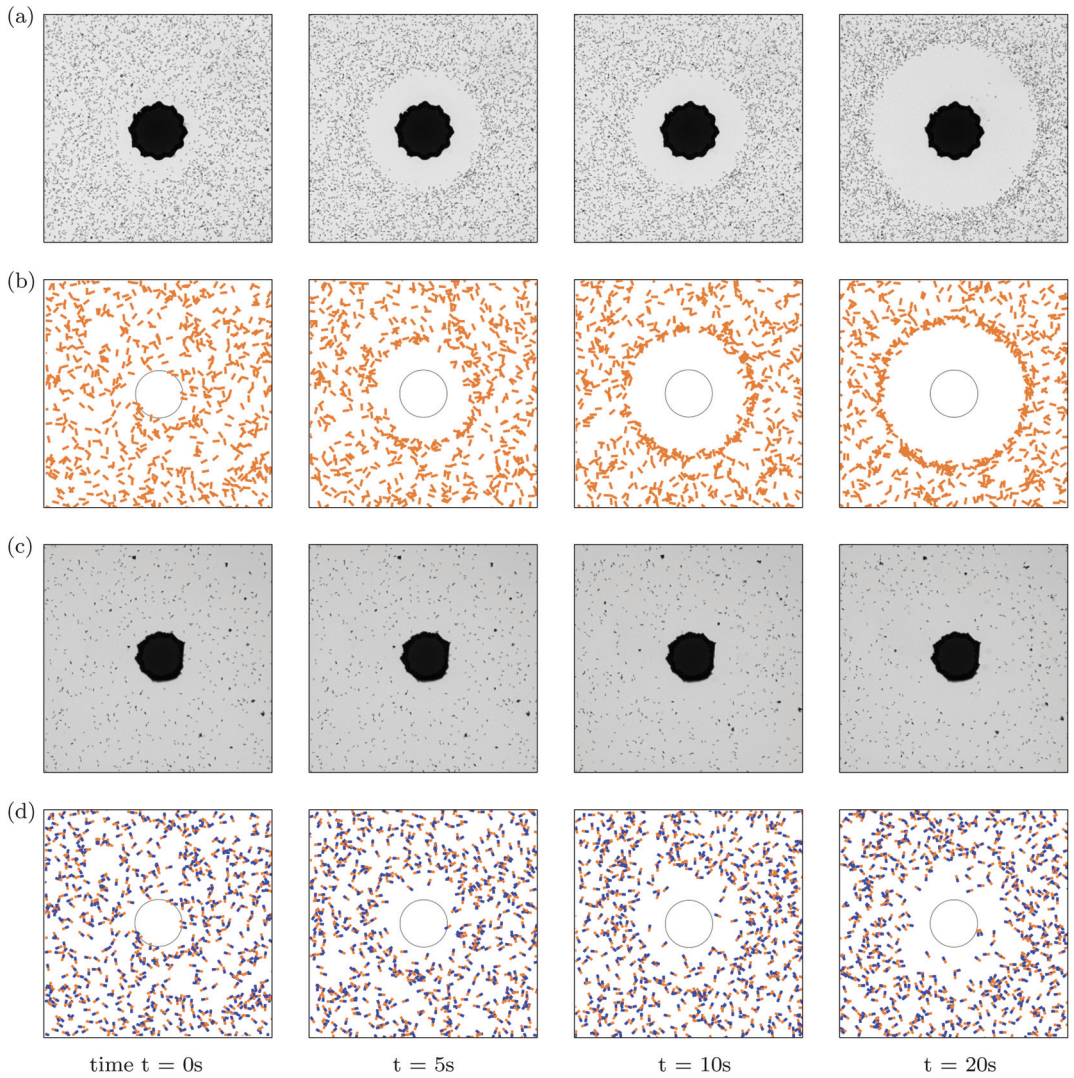

Fig. 4 (color online) Spatiotemporal dynamics of passive tracers (Au microwires): (a) experiment and (b) simulation. Spatiotemporal dynamics of active swimmers (Au–Pt micromotors): (c) experiment and (d) simulation. Also see the accompanying video.

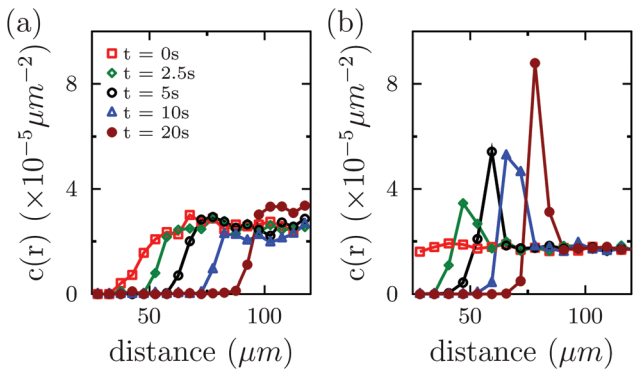

Fig. 5 Passive tracer (Au microwires) density as a function of radial position and time: (a) experiment and (b) simulation.

near the source and the rest of the domain also grows sharper with time. Fig. 3(a) shows the velocity profile of passive tracers for different times. It can be seen that the wires reach a velocity of up to 14 μm s^{-1}. The peak in the velocity is reached very close to the depletion front. The scatter in the passive tracer velocity at any given radial location is a consequence of Brownian fluctuations. Further from the source (≥100 μm), a velocity of 2–4 μm is reported, which corresponds to contributions solely from Brownian motion.

4.2 Active swimmer dynamics

The spatiotemporal dynamics of active swimmers are illustrated in Fig. 4(c) and (d) (and accompanying video). A depletion front advancing radially outward as a result of diffusiophoresis can be clearly seen. However, the depletion effect is reduced by the motility of the swimmers and in particular, the speed acceleration of the micromotors near the source

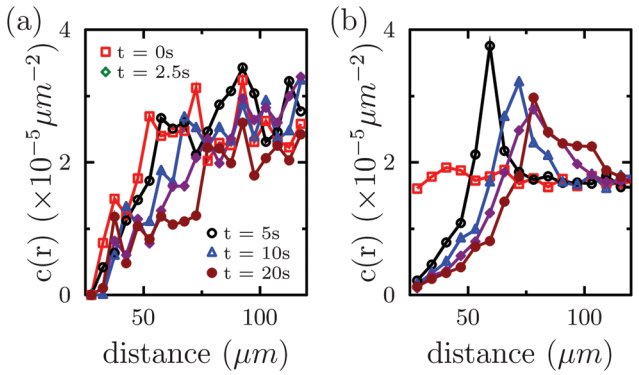

Fig. 6 Active swimmer (Au–Pt micromotor) density as a function of radial position and time: (a) experiment and (b) simulation.

where the silver concentration is high. This near-source acceleration enables the micromotors to overcome the diffusiophoretic flux away from the source and still swim near the source, resulting in a more diffuse interface between the depletion region and rest of the domain. It can be seen from Fig. 3(b) that the micromotors reach velocities up to 30 μm because of the combined effect of silver induced speed acceleration and diffusiophoresis. The peak velocities are always attained closer to the source where the acceleration due to the presence of silver ions is the strongest. The scatter in the velocity data of active swimmers [Fig. 3(b)] at any given radial location is much higher compared to the passive tracers [Fig. 3(a)]. This is because, even while the self-propulsion and diffusiophoretic velocities are only functions of the radial position, the net translational flux is given by their vector sum (as expressed in eqn (2)) and is dependent on the swimmer orientation: swimmers pointing towards the source ($\boldsymbol{p}\cdot\hat{\boldsymbol{e}}_r<0$) have a reduced velocity compared to swimmers pointing away from the source ($\boldsymbol{p}\cdot\hat{\boldsymbol{e}}_r>0$). Because of this effect, the depletion front is found to become more diffuse with time, and the speed at which it advances away from the source is also reduced compared to the case of passive tracer rods as can be seen from Fig. 6.

4.3 Simulation *vs.* experiment

Fig. 4 (and accompanying video) illustrate that the experiments (Fig. 4(a) and (c)) and the Brownian dynamics simulation (Fig. 4(b) and (d)) compare well and the simulations capture all the key qualitative features reported in experiments. The location of the depletion front for both passive tracers and active swimmers [see Fig. 5 and 6(a) *versus* (b)] matches well between experiments and simulations. The only mismatch observed is the presence of the stronger peak in the simulation density profiles, while such clear peaks are absent in the corresponding experimental profiles. This mismatch may be a consequence of several effects, including: the particular way in which the diffusiophoretic velocity is calculated (see section 2); inaccuracies in the diffusion coefficients, which were obtained using slender-body formulas for high-aspect-ratio rods in an unbounded fluid whereas the particles in the experiments reside near a substrate; and the neglect of steric repulsion effects (excluded volume), which likely become important inside the high-density front at the edge of the depletion region. The overall agreement between experiments and simulations, however, validates our modeling approach, assumptions, and silver ion concentration sensing method.

5 Summary

We have applied a combination of experiments and Brownian dynamics simulations to demonstrate the use of both passive and active microrods for the spatial detection of a silver ion source and the accurate spatiotemporal sensing of the resulting silver ion concentration.

First, experiments were performed, where microrods were dropped onto a planar silver ion source. Our experiments revealed that the dynamics can be very different based on whether the microrods are passive or active. Gold microwires, which are passive, progressively move away from the source due to diffusiophoresis in the developing gradient of silver ions. On the other hand, Au–Pt microrods, which are active, also undergo speed acceleration proportional to the silver ion concentration (as has been shown in recent experiments by Kagan *et al.*[27]), which weakens the diffusiophoresis-induced depletion and enables them to swim closer to the source. We note that this is the first experimental study to look at the combined migration and self-propulsion of microparticles when subjected to both externally-imposed and self-generated chemical gradients.

A theoretical model was also proposed based on a simple Langevin equation, accounting for self-propulsion, diffusiophoresis, translational and rotational Brownian motion, coupled with a diffusion equation for silver ion concentration. Our model was shown to have two unknown parameters, *viz.*, the diffusiophoretic coefficient and the surface silver ion flux. Both of these parameters were extracted from two distinct sets of experimental data involving passive and active microrods, respectively. Once these parameters were known, the diffusion equation was analytically solved to obtain the full spatiotemporal evolution of the silver ion concentration in the entire domain, and numerical simulations were performed to integrate the Langevin equation for comparison with the experimental data. Good overall agreement between experiments and simulations was reported. This study, which combined experiments and theory together with passive and active microrods, suggests novel uses for such particles in technological applications requiring biochemical sensing, from chemical threat detection to environmental remediation.

Acknowledgements

This project received support from the Defense Threat Reduction Agency-Joint Science and Technology Office for Chemical and Biological Defense (Grant no. HDTRA1-13-1-0002). D. S. acknowledges support from NSF grant

CBET-1151590. W. G. is a HHMI International Student Research fellow. R. D. acknowledges financial support from the China Scholarship Council (CSC). B. J.-S. acknowledges support from the People Programme (Marie Curie Actions) of the EU 7th Framework Programme (FP7 2007-2013) under REA Grant PIOF-GA-2012-326476. The authors greatly thank Mr Yuri Fedorak for assistance with the preparation of figures.

References

1 J. Palacci, C. Cottin-Bizonne, C. Ybert and L. Bocquet, *Soft Matter*, 2012, **8**, 980.
2 B. Abecassis, C. Cottin-Bizonne, C. Ybert, A. Ajdari and L. Bocquet, *Angew. Chem., Int. Ed.*, 2008, **7**, 785.
3 W. F. Paxton, S. Sundararajan, T. E. Mallouk and A. Sen, *Angew. Chem., Int. Ed.*, 2006, **45**, 5420–5429.
4 W. F. Paxton, K. C. Kistler, C. C. Olmeda, A. Sen, S. K. S. Angelo, Y. Cao, T. E. Mallouk, P. E. Lammert and V. H. Crespi, *J. Am. Chem. Soc.*, 2004, **126**, 13424–13431.
5 G. A. Ozin, I. Manners, S. Fournier-Bidoz and A. Arsenault, *Adv. Mater.*, 2005, **17**, 3011–3018.
6 J. Wang, *Nanomachines: Fundamentals and Applications*, Wiley-VCH, 2013.
7 T. E. Mallouk and A. Sen, *Sci. Am.*, 2009, **300**, 72–77.
8 S. Sanchez and M. Pumera, *Chem. – Asian. J.*, 2009, **4**, 1402–1410.
9 T. Mirkovic, N. S. Zacharia, G. D. Scholes and G. A. Ozin, *ACS Nano*, 2010, **4**, 1782–1789.
10 W. Gao, S. Sattayasamitsathit, J. Orozco and J. Wang, *J. Am. Chem. Soc.*, 2011, **133**, 11862–11864.
11 W. Wang, W. Duan, S. Ahmed, T. E. Mallouk and A. Sen, *Nano Today*, 2013, **8**, 531–554.
12 B. J. Nelson, I. K. Kaliakatsos and J. J. Abbott, *Annu. Rev. Biomed. Eng.*, 2010, **12**, 55–85.
13 K. M. Manesh, S. Balasubramanian and J. Wang, *Chem. Commun.*, 2010, **46**, 5704–5706.
14 S. Balasubramanian, D. Kagan, C.-M. J. Hu, S. Campuzano, M. J. Lobo-Castanon, N. Lim, D. Y. Kang, M. Zimmerman, L. Zhang and J. Wang, *Angew. Chem., Int. Ed.*, 2011, **50**, 4161–4164.
15 S. Campuzano, J. Orozco, D. Kagan, M. Guix, W. Gao, S. Sattayasamitsathit, J. C. Claussen, A. Merkoi and J. Wang, *Nano Lett.*, 2012, **12**, 396–401.
16 J. Wang and W. Gao, *ACS Nano*, 2012, **6**, 5745–5751.
17 T. Petit, L. Zhang, K. E. Peyer, B. E. Kratochvil and B. J. Nelson, *Nano Lett.*, 2012, **12**, 156–160.
18 J. Orozco, V. Garcia-Gradilla, M. DÁgostino, W. Gao and J. Wang, *ACS Nano*, 2013, **7**, 818–824.
19 M. Guix, J. Orozco, M. Garcia, W. Gao, S. Sattayasamitsathit, A. Merkoci, A. Escarpa and J. Wang, *ACS Nano*, 2012, **6**, 4445–4451.
20 W. Gao, X. Feng, A. Pei, Y. Gu, J. Li and J. Wang, *Nanoscale*, 2013, **5**, 4696–4700.
21 J. Orozco, G. Cheng, D. Vilela, S. Sattayasamitsathit, R. Vazquez-Duhalt, G. Valdes-Ramirez, O. S. Pak, A. Escarpa, C. Kan and J. Wang, *Angew. Chem., Int. Ed.*, 2013, **52**, 13276–13279.
22 L. Soler, V. Magdanz, V. M. Fomin, S. Sanchez and O. G. Schmidt, *Angew. Chem., Int. Ed.*, 2013, **7**, 9611–9620.
23 J. G. S. Moo, H. Wang, G. Zhao and M. Pumera, *Chem. – Eur. J*, 2014, **20**, 4292–4296.
24 W. Gao and J. Wang, *ACS Nano*, 2014, **8**, 3170–3180.
25 W. Gao, A. Pei, R. Dong and J. Wang, *J. Am. Chem. Soc.*, 2014, **136**, 2276–2279.
26 Y. Hong, N. M. K. Blackman, N. D. Kopp, A. Sen and D. Velegol, *Phys. Rev. Lett.*, 2007, **99**, 178103.
27 D. Kagan, P. Calvo-Marzal, S. Sattayasamitsathit, K. M. Manesh, G.-U. Flechsig and J. Wang, *J. Am. Chem. Soc.*, 2009, **131**, 12082–12083.
28 J. Wu, S. Balasubramanian, D. Kagan, K. M. Manesh, S. Campuzano and J. Wang, *Nat. Commun.*, 2010, **1**, 36.
29 D. C. Prieve, J. L. Anderson, J. P. Ebel and M. E. Lowell, *J. Fluid Mech.*, 1984, **148**, 247–269.
30 J. L. Anderson, *Annu. Rev. Fluid Mech.*, 1989, **21**, 61–99.
31 M. Doi and S. F. Edwards, *The Theory of Polymer Dynamics*, Oxford University Press, 1986.
32 J. Palacci, B. Abecassis, C. Cottin-Bizonne, C. Ybert and L. Bocquet, *Phys. Rev. Lett.*, 2010, **104**, 138302.
33 Y. Hong, M. Diaz, U. M. C. Figueroa, A. Sen and D. Velegol, *Adv. Funct. Mater.*, 2010, **20**, 1568–1576.

